Energy &
Environmental
Science

The Role of Atomic Carbon in Directing Electrochemical CO$_2$ Reduction to Multicarbon Products

Journal:	*Energy & Environmental Science*
Manuscript ID	EE-ART-09-2020-002826.R2
Article Type:	Paper
Date Submitted by the Author:	16-Nov-2020
Complete List of Authors:	Peng, Hongjie; SLAC National Accelerator Laboratory, SUNCAT Center for Interface Science and Catalysis; Stanford University, Department of Chemical Engineering, SUNCAT Center for Interface Science and Catalysis Tang, Michael; Stanford University, Department of Chemical Engineering, SUNCAT Center for Interface Science and Catalysis; Stanford University, Department of Materials Science Engineering Liu, Xinyan; SLAC National Accelerator Laboratory, SUNCAT Center for Interface Science and Catalysis; Stanford University, Department of Chemical Engineering, SUNCAT Center for Interface Science and Catalysis Schlexer Lamoureux, Philomena; SLAC National Accelerator Laboratory, SUNCAT Center for Interface Science and Catalysis; Stanford University, Department of Chemical Engineering, SUNCAT Center for Interface Science and Catalysis Bajdich, Michal; SLAC National Accelerator Laboratory, SUNCAT Center for Interface Science and Catalysis Abild-Pedersen, Frank; SLAC National Accelerator Laboratory, SUNCAT Center for Interface Science and Catalysis

SCHOLARONE™
Manuscripts

The Role of Atomic Carbon in Directing Electrochemical $CO_{(2)}$ Reduction to Multicarbon Products

Hongjie Peng[1, 2, 4], Michael T. Tang[2, 3, 4], Xinyan Liu[1, 2],
Philomena Schlexer Lamoureux[1, 2], Michal Bajdich[1] and Frank Abild-Pedersen[1,*]

[1] *SUNCAT Center for Interface Science and Catalysis,*
SLAC National Accelerator Laboratory,
California 94025, USA

[2] *SUNCAT Center for Interface Science and Catalysis,*
Department of Chemical Engineering,
Stanford University, California 94305, USA

[3] *Department of Material Science and Engineering,*
Stanford University, California 94305, USA

[4] *These authors contributed equally: Hongjie Peng, Michael T. Tang.*

* Corresponding Author email: abild@slac.stanford.edu

Abstract

Electrochemical reduction of carbon-dioxide/carbon-monoxide ($CO_{(2)}R$) to fuels and chemicals presents an attractive approach for sustainable chemical synthesis, but it also poses a serious challenge in catalysis. Understanding the key aspects that guide $CO_{(2)}R$ towards value-added multicarbon (C_{2+}) products is imperative in designing an efficient catalyst. Herein, we identify the critical steps toward C_2 products on copper through a combination of energetics from density functional theory and micro-kinetic modeling. We elucidate the importance of atomic carbon in directing C_{2+} selectivity and how it introduces surface structural sensitivity on copper catalysts. This insight enables us to propose two simple thermodynamic descriptors that effectively identify C_{2+} selectivity on metal catalysts beyond copper and hence it defines an intelligible protocol to screen for materials that selectively catalyze $CO_{(2)}$ to C_{2+} products.

Introduction

The electrochemical reduction of CO_2 and CO paves a promising pathway towards sustainable chemicals and fuels.[1, 2] The mechanism that drives the generation of high-value multicarbon (C_{2+}) products is of particular interest but despite many years of research it still remains elusive.[3] So far elemental copper (Cu) and Cu-based compounds are the only materials that can produce $C_{2(+)}$ hydrocarbons and oxygenates of any significance albeit at high overpotential and with poor selectivity.[4] To optimize Cu-based catalysts or find alternative materials for selective $C_{2(+)}$ production from $CO_{(2)}$, in-depth mechanistic insight is needed in order to unravel the complexities of $CO_{(2)}R$.[5]

Recent experimental efforts have focused on improving the selectivity towards $C_{2(+)}$ products on Cu by tailoring catalyst composition,[6-10] the surface morphology,[11-14] the reaction conditions at the catalyst/electrode interface,[15-18] and by engineering the electrochemical reactors.[19-22] To identify key intermediates and tie that into theoretical efforts, *in situ* or *operando* characterization tools have been employed,[23-25] but the precise mechanism of the first C–C bond formation is still inconclusive. Inspired by an experimentally observed larger shift in onset potential with pH for C_2 than C_1 products,[26-28] theoretical work has concentrated on coupling steps early in the reduction pathway, in particular CO dimerization.[29-34] The CO dimerization step is strongly affected by solvation and the electric field present at the electrochemical interface,[30, 35, 36] which introduces extra complexity that hinders descriptor-based materials discovery beyond Cu-based catalysts.[10]

In this work, we investigate the critical steps of CO reduction (COR) toward C_2 products with density functional theory (DFT) based reaction and activation energies and introduce an electrochemical microkinetic model that appropriately describes the experimental trends in activity and selectivity. Our model (exemplified on Cu(100)) identifies a potential, U_0, at which the reduction of CO to atomic carbon (C*) via the COH* intermediate exhibits higher rate than both the hydrogen evolution reaction (HER) and the reduction of CO to CHO*. Subsequently, the surface C* enables thermodynamically favorable coupling with CO at the interface. In comparison with other pathways including CO dimerization, this process is found to be the dominant C_2 pathway at more reducing potentials, *i.e.*, $U < -0.5$ V vs. the reversible hydrogen electrode (RHE) at pH = 7. This enables a characterization of the C_2 selectivity relative to the single-carbon (C_1) selectivity

through the energetic difference between barriers for CCO* and CH* formation, which further rationalizes the facet dependency of C_2 selectivity on Cu. Finally, this insight allows us to identify two simple descriptors that traces the C_2 selectivity on different metal surfaces at varying potentials: the adsorption free energies of CO* and C* (G_{CO*} and G_{C*}).

Results and Discussion

Reaction pathways for COR

In this paper, we evaluate the CO_2R reaction to C_1 and $C_{2(+)}$ products involving more than two proton-electron transfer steps with water as the proton donor. It has been verified that CO* is the most important common intermediate in COR and CO_2R leading to further reduced products,[4, 26] we therefore focus on CO as the initial reactant. Since Cu is the only catalyst with significant $C_{2(+)}$ production from $CO_{(2)}$ and its (100) surface has been identified as the major exposed facet under reaction conditions,[12, 37] we select Cu(100) as the model surface. All the computational details and the simplifications of the electrochemical models are shown in **Supplementary Note** with corresponding data and justification present in **Figures S1–S6** and **Tables S1–S9**.
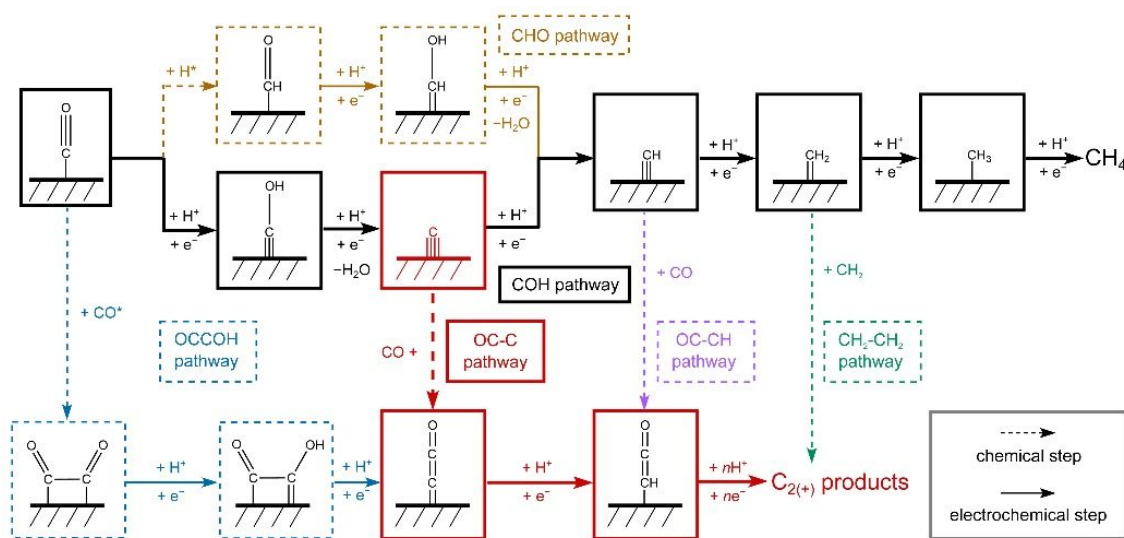
Figure 1. Schematic diagram of reaction steps beyond CO. Pathways toward C_1 (CH_4 as the main product) and C_2 products beyond CO are shown as different colored branches: yellow (CHO pathway), black (COH pathway), blue (OCCOH pathway), red (OC-C pathway), violet (OC-CH pathway), and green (CH_2-CH_2 pathway). The number of involved reduction steps are increasing from left to right.

Figure 1 shows the most relevant reactions considered in this work. Clearly, CO* is initially reduced to either CHO* or COH*. In a recent study,[38] we showed that the formation of CHO* is a chemical step preceded by surface hydrogenation whereas COH* is formed through an electrochemical reduction step. CH* leading to CH_4 forms as an intermediate in both pathways, either via COH reduction to C* + H_2O or through CHO reduction to CHOH*. A number of intermediates present in the CH_4 pathway are considered as seeds for $C_{2(+)}$ production: CO* dimerization to OCCO* and subsequent reduction to OCCOH* (OCCOH pathway), CO* coupling with C* (OC-C pathway), CO* coupling with CH* (OC-CH pathway), and CH_2* dimerization to ethylene (C_2H_4) (CH_2-CH_2 pathway). In accordance with previous studies, we only consider OCCOH* as the reduced product of OCCO*.[29, 32, 33, 35] Potential coupling reactions of CO with either CHO* or COH* are compared with the OCCOH pathway in the next section. The above considered C_2 pathways except for the CH_2 dimerization lead to CHCO* and based on previous thermodynamic analyses,[29] all subsequent reaction steps are assumed to be downhill in energy.

Figures 2a–e depicts the Gibbs free energetics of competing pathways, as proposed in **Figure 1**, at two applied potentials vs. RHE on Cu(100). $U_{RHE} = -0.13$ V was chosen as it corresponds to the zero-charge potential of Cu(100) at pH=7, showing the energetics un-affected by fields; while $U_{RHE} = -0.73$ V was chosen as it is the value at which substantial $C_{2(+)}$ products begin forming on Cu in neutral-pH $CO_{(2)}$R.[26, 27, 39] Cation-induced interfacial fields have been suggested to significantly stabilize C_2 species like OCCO*.[13, 30, 36] Given these previous insights, we have built a simple model (see details in **Supplementary Note 4**) to correlate the field-affected energetics to the potentials vs. the standard hydrogen electrode (SHE), which we denote as U_{SHE}. For all chemical steps the adsorption energies at $U_{RHE} = 0$ V and barriers were calculated in vacuum and all electrochemical barriers were obtained using an explicit solvent model combined with the charge-extrapolation method.[40] Free-energy and solvation corrections were applied to adsorption energies for all important intermediate species (**Table S3** and **Table S4**). The relevant transition state (TS) structures are shown in **Figure 2f**.
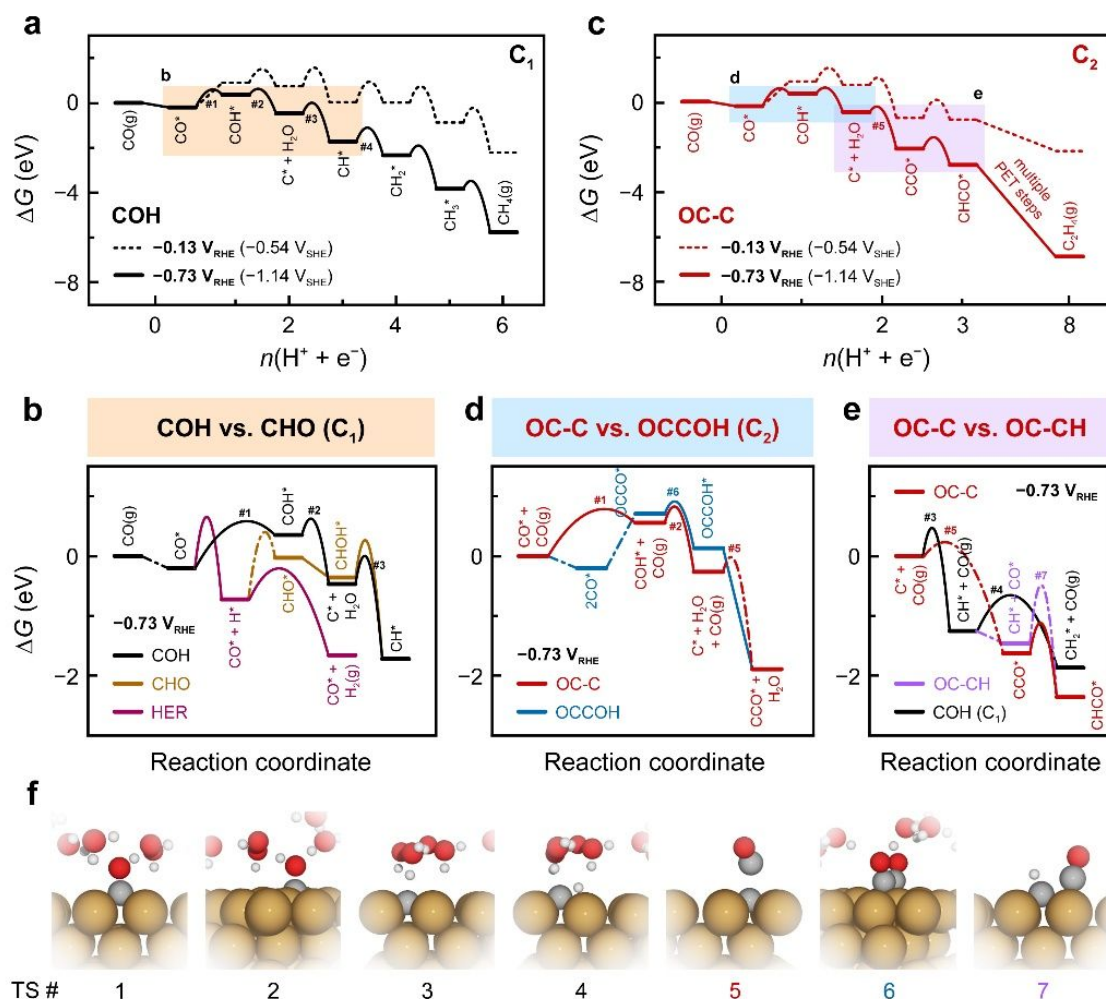
Figure 2. Free energy diagrams (FEDs) of COR on Cu(100) at pH7. FEDs at potentials U_{RHE} = −0.13 V and U_{RHE} = −0.73 V, showing (**a**) the COH pathway toward CH_4 and (**c**) the OC-C pathway toward C_2 pathway where C_2H_4 is used as the representative product. The colored squares highlights the major steps competing with other pathways at potential U_{RHE} = −0.73 V: (**b**) COH (black), CHO (brown), and HER (wine); (**d**) OC-C (red) and OCCOH (blue); (**e**) OC-CH (violet) and COH toward C_1 (black). Note that the scale of the *x*-axes in (**a**) and (**c**) are non-uniform due to the presence of chemical steps. These chemical steps are shown as the dash-dotted lines in (**b**, **d**, and **e**). (**f**) TS structures of key elementary steps with the indexes indicated in (**a**–**e**): 1. CO-H to COH*, (2) COH-H to C* + H_2O, (3) C-H to CH*, (4) CH-H to CH_2*, (5) C-CO coupling, (6) OCCO-H to OCCOH*, and (7) OC-CH coupling.

At low overpotentials, the formation of C* + H_2O through sequential CO-H and COH-H protonation is identified to control the overall rate of the COH pathway (**Figure 2a**). With increasing overpotential, the CO-H protonation is shown as the rate-determining step (RDS) with a lower barrier than both the HER and the CHO pathway (**Figure 2b**) and thus the COH pathway is more favorable within a wide potential window (**Figure S7**).

5

Therefore, C* becomes available on the surface under these conditions, opening up pathways leading to C_1 products through further protonation (**Figure 2a**) or C_2 products via coupling with CO (**Figure 2c**). On Cu(100) CO binds at least −1.25 eV stronger to C* than the surface throughout the common potential range (**Figure S8**). In addition, C* coupling to gas-phase CO possesses a barrier of 0.31 eV, which is lower than the 0.73 eV for the surface mediated coupling (**Figure S9**). The energetics agrees well with observed facile low-temperature CO dissociation on Cu induced by C-CO coupling.[41] With an additional stabilization of C-CO TS by the interfacial field, the CCO formation from C* is more favorable at low overpotentials than the CH formation, thus resolving the earlier onset potentials for C_2 than for C_1 in $CO_{(2)}R$.[26, 27, 39]

As mentioned in **Figure 1,** several possible competing carbon-coupling pathways are considered. The rate of the OCCOH pathway is identified to be largely controlled by CO dimerization and subsequent protonation (**Figure S10**). Despite the significant field stabilization of OCCO* and OCCOH*, this conventional pathway is found to possess higher activation energies than the COH/OC-C pathway, thereby being less dominant at sufficiently negative potentials (**Figure 2d**). In addition, the OCCOH pathway is found to be more predominant than other coupling reactions early in the reduction pathway, such as OC-COH and OC-CHO coupling (**Figure S11**). Owing to the higher coupling barriers than the protonation barriers at negative potentials, the OC-CH and CH_2 dimerization pathways cannot compete with their protonation counterparts of CH-H and CH_2-H, respectively (**Figure 2e** and **Figure S12**).

Microkinetic model of COR

To further illustrate the role of C* as a potential bifurcating intermediate for C_1/C_{2+} products, we have developed a mean-field microkinetic model that consider adsorbate-adsorbate interactions.[35] Given the intrinsic DFT errors (±0.15 eV) and the uncertainties brought by the parameterization and the variations in the solvent structure, the microkinetic model only serves as a tool for qualitative comparison with experimental trends in activity and selectivity.
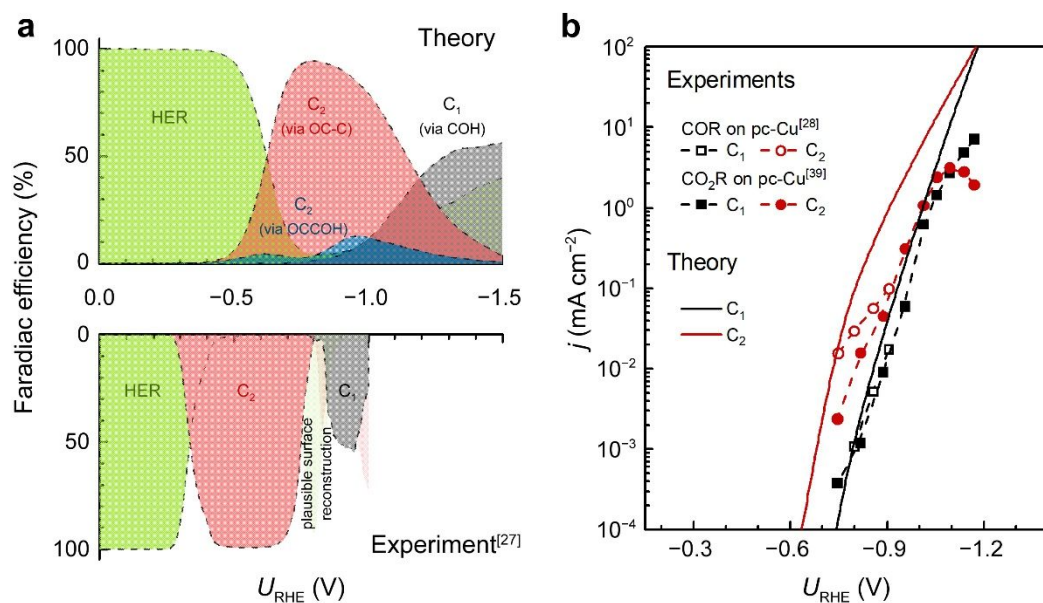
Figure 3. Product distributions and polarization curves of $CO_{(2)}R$ on Cu(100) (bulk pH7). (a) Theoretical (top) and experimental (bottom) distributions of products. The experimental product distribution for COR on a Cu(100) single-crystal electrode was from Koper et al.[27] The HER and C_2 activity at $U_{RHE} < -0.7$ V is hypothesized to result from potential-driven surface reconstruction.[27] **(b)** The comparison between theoretical COR and experimental $CO_{(2)}R$ polarization curves. The experimental curves for COR and CO_2R are obtained on pc-Cu from Ref. [28] and Ref. [39], respectively.

Figure 3a shows the product distribution from the microkinetic model at bulk pH=7 across a wide range of potentials vs. RHE. The distribution aligns well with the trends seen in experiments.[27] The partial contributions from each pathway as shown in **Figure S13** is a reflection of the free energetics shown in the last section, identifying the COH pathway and the OC-C pathway as the two dominant pathways that lead to C_1 and C_2 products, respectively.

Further comparison with the experimental polarization curves of COR and CO_2R on polycrystalline Cu (pc-Cu) electrodes underscores the ability of our proposed model to accurately predict the potential-dependent variations in activity and selectivity (**Figure 3b**). The observed experimental downward trend of C_2 formation seen in **Figure 3b** can be attributed to the CO depletion induced by mass transport limitation.[35]

We note that under steady-state conditions, CO* is the major surface species (**Figure S14**). Therefore, stronger CO* adsorption on step sites combined with a low step formation energy on Cu could drive possible surface reconstruction of Cu(100).[42] Nevertheless, a comparison of our microkinetic model with previously established ones on stepped

surfaces[35, 43] show similar accuracy in describing the $CO_{(2)}R$ trends on pc-Cu. While the C* intermediate has been proposed previously,[26, 31, 44] none of the previous models have revealed the particular OC-C coupling mechanism leading to C_{2+}.

pH effects

To understand the observed correlations between C_{2+} selectivity and bulk pH, we also consider COR under experimental alkaline conditions (0.1 M KOH, $pH_{bulk} = 13$;[18, 27, 28] and 5 M KOH, $pH_{bulk} = 14.7$[22]). Our model shows that the dominant region for the OCCOH mechanism expands on the U_{SHE} scale with increasing alkalinity (**Figure 4a**). Previous understanding of the alkaline protonation process revealed that electrochemical barriers are dependent on the U_{SHE} while reaction energies are U_{RHE}-dependent.[35] Therefore, the potential required to drive C* formation shifts more negative with increasing pH_{bulk} due to the additional reduction step needed than for OCCOH* formation. A detailed degree-of-rate-control analysis[45] also reveals such a transition in the dominant reaction pathways (**Figure S15**). In short, from a neutral pH_{bulk} to an alkaline pH_{bulk} of around 13, we suggest that the experimentally observed large shifts in pH of C_{2+} activity/selectivity in **Figure 4b** and **4c** can be rationalized by the OCCOH pathway being dominant at low overpotentials, whereas the COH/OC-C pathway only become relevant at high overpotential.

Recent developments in $CO_{(2)}R$ reactors has promoted $CO_{(2)}R$ current densities to 10^2–10^3 mA cm^{-2}, which generate a high local pH of around 10–11.[1, 14, 19-22] To show the reliability of our model for such systems, we also simulated COR at a pH_{bulk} of 7 and local pH ($pH_{interface}$) of 9 and 11 according to recent efforts in modeling[14, 46] and characterization.[25] Due to the independency of absolute potential at the working electrode on local pH, the high local pH only destabilizes the final state of each reduction step by $0.059\Delta pH$ at 298K (**Figure S16a**). As long as the RDS is the first protonation step (CO-H and OCCO-H protonation identified in **Figure S15**), the reaction rate remains the same. Therefore, similar to the change in pH_{bulk}, the increased local alkalinity only results in more negative potentials required to switch the dominant C_2 reaction pathways from the OCCOH to the OC-C (**Figure S16b** and **S16c**); whereas the overall trends of COR within the potential window of interest (usually $U_{RHE} < -0.8$ V to obtain a sufficiently high $pH_{interface}$ of > 9 in neutral electrolytes) still reveals a dominance of the OC-C pathway for C_2

production and hence consistent with the neutral-pH_{bulk} model (**Figure S17**). The observed dependency of C_{2+} selectivity on the $pH_{interface}$ could also be attributed to different CO_2 concentrations.[15, 25] Regardless of local pH effects, C* becomes the key intermediate that directs C_1 and C_2 selectivity on Cu below a certain potential.
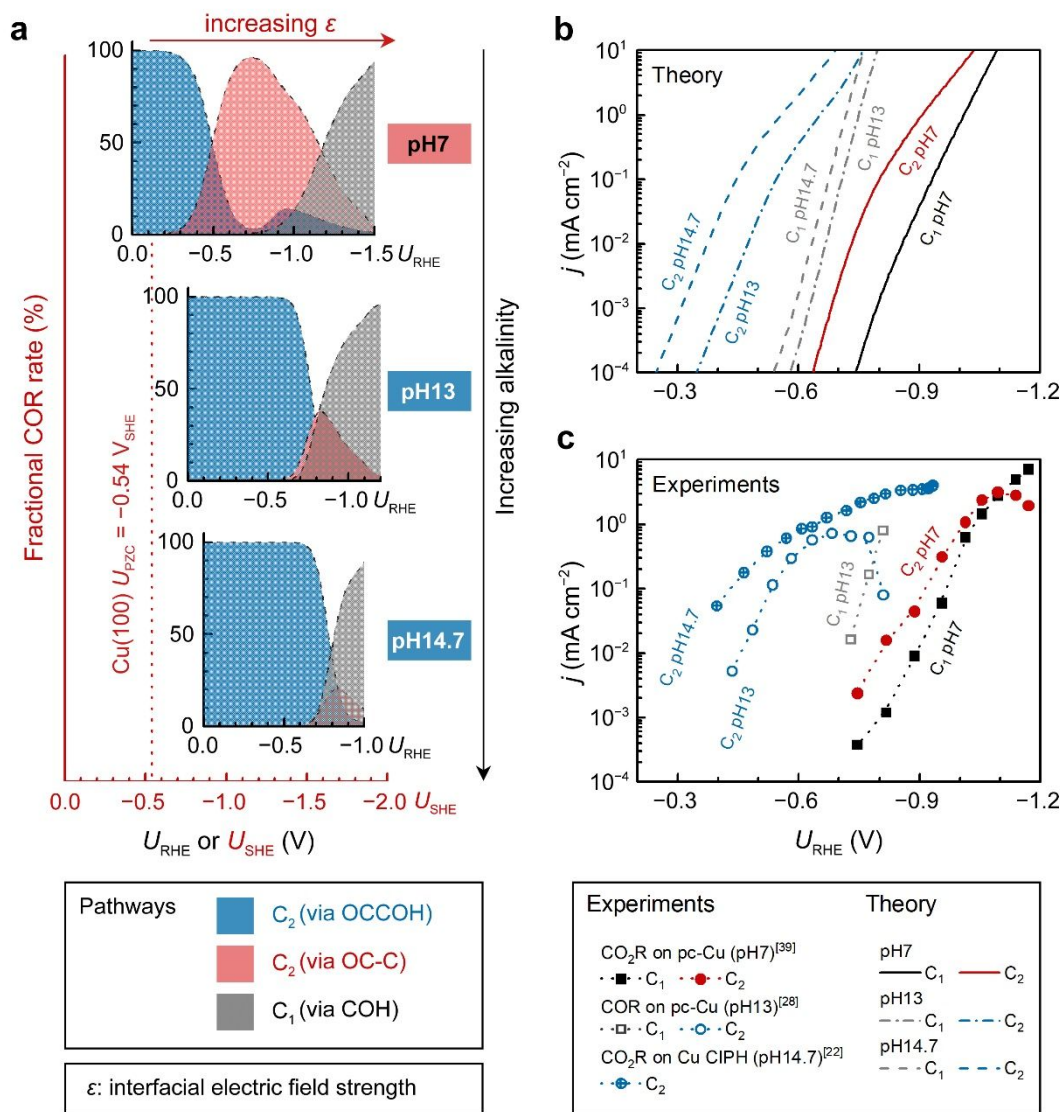
Figure 4. Product distributions and polarization curves of $CO_{(2)}R$ on Cu(100) under different bulk pH (pH_{bulk}) conditions. (**a**) Fractional COR rates (by normalizing to the total COR rate) from three pathways: OCCOH to C_2 (blue), OC-C to C_2 (red), and COH to C_1 (gray). The pH_{bulk} increases from top to the bottom. (**b**) Theoretical polarization curves. (**c**) Experimental polarization curves of COR and CO_2R are obtained on pc-Cu from Ref. [39] (0.1 M KOH), Ref. [28] (0.1 M KHCO$_3$), and on Cu catalyst-ionomer planar heterojunction (CIPH) from Ref.[22] (5 M KOH), respectively. Note that the current densities obtained from Ref.[22] were normalized to electrochemical specific area.

Through the above analysis, we clarify that the proposed OC-C pathway is not in conflict with the CO dimerization pathway at low overpotentials. In fact, both the OC-C and CO dimerization steps are important for the mechanistic understanding and the development of practical solutions. Besides, the electric field effect on the CO dimerization to rationalize the local-field-dependent C_{2+} selectivity still holds based on the OC-C pathway due to the field stabilization to C-CO^{TS}.[15, 16] Engineering parameters in our field model such as $\Phi_{M, PZC}$ and d could be feasible strategies to increase the C_2 selectivity.[36] In brief, by combining competing reaction pathways and specific pH/interface conditions our model provides reasonable agreement with experimental observation and it shows the importance of including the OC-C pathway in the overall $CO_{(2)}R$ mechanism.

Facet dependent selectivity of C₂ on Cu

Our approach and microkinetic modeling enables us to identify four key reaction steps that determines the $CO_{(2)}R$ activity and selectivity:

(i) CO^* (or $CO(g) + *$) $+ H^+ + e^- \rightarrow COH^*$ (CO-H protonation)

(ii) CO^* (or $CO(g) + *$) $+ 2(H^+ + e^-) \rightarrow C^* + H_2O$ (C formation)

(iii) $CO(g)$ (or CO^*) $+ C^* \rightarrow CCO^*$ (C-CO coupling)

(iv) $C^* + H^+ + e^- \rightarrow CH^*$ (C-H protonation)

Here reaction (i) and (ii) determine the overall rate which explicitly accounts for the shift in RDS with applied potential. The competition between reaction (iii) and (iv) determine the selectivity.
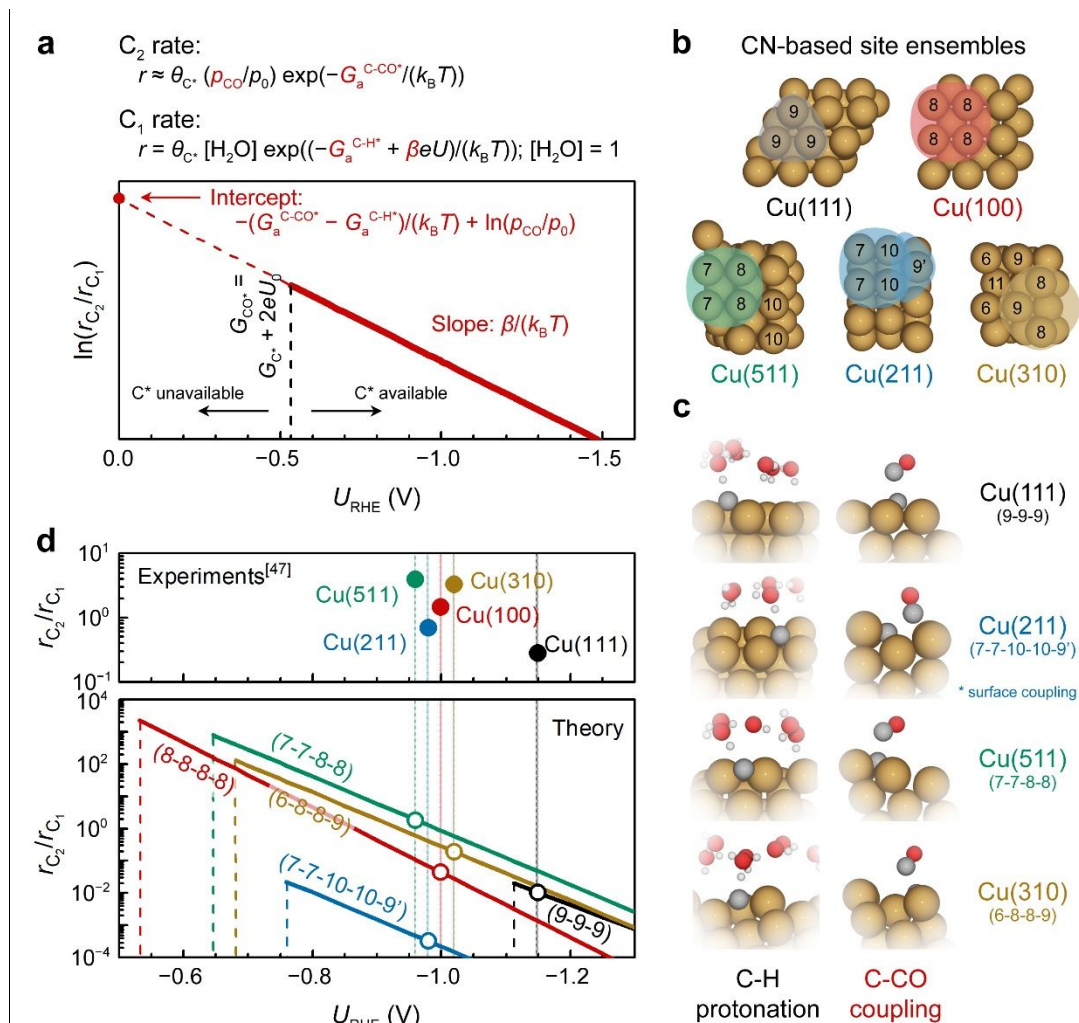
Figure 5. Facet dependent selectivity of C_2 on Cu (pH7). (**a**) Schematic illustration of the potential-dependent C_2 selectivity over a certain facet, showing the expression for onset potential U_0, slope, and intercept. (**b**) Site ensembles defined by their local CNs on (111), (211), (511), (100), and (310) facets of Cu. (**c**) TS structures of C-H protonation and C-CO coupling on the site ensembles shown in **b**. (**d**) Potential-dependent C_2 selectivity on the representative site ensemble of (111), (211), (511), (100), and (310) facets of Cu. Vertical dash lines indicate the onset potential U_0 for CO protonation and hence the formation of C* on the surface. The experimental numbers for r_{C_2}/r_{C_1} are obtained from Ref.[47] on various single-crystal Cu electrodes. The light vertical lines indicate the experimental applied potential for long-term electrolysis experiments. (* On Cu(211), CO* couples with C* via a surface mediated mechanism due to a geometric constraint; thus, the intercept in (**a**) is expressed as $\ln(\theta_{CO*}) + \dfrac{-G_a^{OC\text{-}C} + G_a^{C\text{-}H}}{k_B T}$ for Cu(211). 9' in the site ensemble of 7-7-10-10-9' represents the binding site of CO*.).

Based on our microkinetic model and a simple quasi-equilibrium assumption, surface C* will become accessible at a certain potential, U_0, defined by the condition; $\Delta G^{(ii)}_{rxn} = 0$. According to the computational hydrogen electrode model,[48] U_0 is defined as $(G_{C*} - G_{CO*}$ (or $G_{CO(g)}))/(-2e)$. When $U < U_0$, the forward rates of reaction (iii) and reaction (iv) are

given by:

$$r_{C_2} = A\theta_{C*}\theta_{CO*}\exp\left(-\frac{G_a^{OC\text{-}C}}{k_BT}\right) + A\theta_{C*}\left(\frac{p_{CO}}{p_0}\right)\exp\left(-\frac{G_a^{C\text{-}CO}}{k_BT}\right)$$

$$r_{C_1} = A\theta_{C*}[H_2O]\exp\left(-\frac{G_a^{C\text{-}H} + e\beta U_{RHE}}{k_BT}\right)$$

where A is a pre-exponential factor, k_B Boltzmann's constant, T the absolute temperature, θ_{C*} and θ_{CO*} are surface coverages of C* and CO*, respectively, (p_{CO}/p_0) is the partial pressure of gas-phase CO, and $G_a^{OC\text{-}C}$, $G_a^{C\text{-}CO}$, and $G_a^{C\text{-}H}$ are forward activation energies of OC-C surface coupling, C-CO gas-phase coupling, and C-H protonation at $U_{RHE} = 0$ V, respectively. The charge transfer coefficients for the C-H protonation step, β, vary from 0.45 to 0.60 depending on the surface orientation (see **Table 1**). Since both $\Delta G^{(iii)}_{rxn}$ and $\Delta G^{(iv)}_{rxn}$ are considerably downhill in energy when $U < U_0$, only the forward rates are taken into account. According to a previous analysis,[49] we only regard molecular water as the proton donor within the relevant pH range (pH > 4), at which $[H_2O] = 1$ is a reasonable assumption. In this study, all facets Cu(100), Cu(111), Cu(511), Cu(310), except for Cu(211) exhibit much larger $G_a^{OC\text{-}C}$ than $G_a^{C\text{-}CO}$ (see **Table 1**), hence the expression for the C$_2$ rate is simplified when omitting the first term such that:

$$r_{C_2} \approx A\theta_{C*}\left(\frac{p_{CO}}{p_0}\right)\exp\left(-\frac{G_a^{C\text{-}CO}}{k_BT}\right)$$

If we assume similar pre-exponential factors for the two reaction steps, the selectivity of C$_2$ over C$_1$ can be expressed as:

$$\ln\left(\frac{r_{C_2}}{r_{C_1}}\right) \approx \ln\left(\frac{p_{CO}}{p_0}\right) + \frac{-G_a^{C\text{-}CO} + G_a^{C\text{-}H} - e\beta U_{RHE}}{k_BT}$$

This result enables a quantitative assessment of the slope and intercept of $\ln(r_{C_2}/r_{C_1})$ on a certain type of active site as well as the mapping of selectivity as a function of potential (**Figure 5a**). Note that CO partial pressure is assumed to be 0.05 bar for all Cu facets, the same as what is applied during the microkinetic modeling for consistency. The accurate determination of the CO partial pressure at the reaction interface requires additional multiscale simulations explicitly considering mass transport. The typical site ensembles of different Cu facets are shown in **Figure 5b** based on their local coordination number (CN).

Table 1. A summary of the G_a^{OC-C}, G_a^{C-CO}, G_a^{C-H}, and β_{C-H} on various Cu facets.

Cu facets	Site ensembles	G_a^{OC-C} (eV)	G_a^{C-CO} (eV)	G_a^{C-H} (eV)	β_{C-H}
(100)	(8-8-8-8)	0.73	0.31	0.91	0.60
(111)	(9-9-9)	---	0.15	0.63	0.45
(211)	(7-7-10-10-9')	0.46	---	0.80	0.50
(511)	(7-7-8-8)	0.49	0.27	0.84	0.50
(310)	(6-8-8-9)	0.69	0.30	0.85	0.50

Note: the OC-C barrier calculation on Cu(111) and C-CO barrier calculation on Cu(211) automatically relax to the C-CO and OC-C mechanism, respectively. For simplicity, the energetics considered for facet dependency are without field correction.

Since the TS structures shown in **Figure 5c** are very similar on different site ensembles, the above expression possesses certain generality. **Figure 5d** depicts the theoretical trends in C_2 selectivity on different Cu site ensembles. Typical four-fold hollow sites such as (8-8-8-8), (7-7-8-8), and (6-8-8-9) are very selective towards C_2 at low overpotentials (−0.7 to −0.9 V). The (7-7-10-10-9') site is seen to have a higher barrier, G_a^{OC-C}, compared to the other facets and therefore it is less selective, whereas the typical three-fold hollow site of (9-9-9) possesses a low G_a^{C-CO} which automatically result in a favored C_2 selectivity. However, the instability of C* limits the (9-9-9) site, which results in a much lower U_0 compared to the other site ensembles and thus an inferior C_2-selectivity. Due to weaker binding of C* on Cu(111) an additional C_1 pathway becomes possible in which the protonation of COH* to CHOH* is favored over C* formation thus providing an increased C_1 activity on the Cu(111) surface and an overall lower experimental r_{C_2}/r_{C_1}.[32] Overall, the observed facet dependency is rationalized by the greater stabilization of atomic C* on Cu (100)-like sites. This characteristic four-fold geometry combined with the unique electronic structures of Cu is what causes the favored selectivity of C_2 over C_1 products. These trends are in good agreement with experimentally observed facet dependencies by Hori et al.,[47] demonstrating the ability of our model to describe structure sensitivity for $CO_{(2)}R$ catalysts.

The facet dependency insight achieved through the simple expression of $\ln(r_{C_2}/r_{C_1})$ above, also offers several strategies to enhance the C_{2+} selectivity by tuning the effective

CO pressure/concentration, including system pressurization,[28] CO/CO_2 co-feeding,[50] and doing the electrocatalysis in tandem[9, 50].

Selectivity maps with G_{CO*} and G_{C*} as descriptors

We note that the energetic analysis through reactions (i)–(iv) is sufficient to qualitatively unveil the trends in $CO_{(2)}R$ activity and selectivity. Considering that their reaction energies can be adequately described through scaling by G_{CO*} and G_{C*} (**Figure S18**), we can therefore create a selectivity map across various metals. To show the importance of four-fold sites in stabilizing C*, we include the (100), (111), (211) facets on close-packed metals. Similar maps using binding strengths of CO and OH as descriptors for selectivity towards C_1 products have been introduced recently.[38]

   As shown in **Figure 6**, the map uses simple thermodynamic conditions based on the reaction energies (ΔG_{rxn}) for reactions (i)–(iv):

CO to COH* acceptable rate (TOF 1 s^{-1} $site^{-1}$ at 300K): $\Delta G^{(i)}_{rxn} < 0.75$ eV   (Eq. 1)

CO reduction to kinetically accessible C*: $\Delta G^{(ii)}_{rxn} = 0$ (Eq. 2)

C-CO coupling more favorable than CO adsorption: $\Delta G^{(iii)}_{rxn} < G_{CO*}$ (Eq. 3)

C-CO coupling more favorable than C-H protonation: $\Delta G^{(iv)}_{rxn} < \Delta G^{(iii)}_{rxn}$ (Eq. 4)

Since CO-H protonation eventually becomes the RDS of $CO_{(2)}R$ (**Figure S15**), we therefore use $\Delta G^{(i)}_{rxn}$ as an estimate of the barrier for the RDS and assign a turnover frequency of ~1 s^{-1} per site at 300K as the lowest acceptable overall $CO_{(2)}R$ rate. Such a rate corresponds to the condition defined by Eq. 1. To accurately describe the effect of CO adsorption, we replace G_{CO*} in Eqs. (1–3) with $G_{CO} = 0$ when the adsorption of CO on the catalytic surface is unfavorable ($G_{CO*} > 0$).
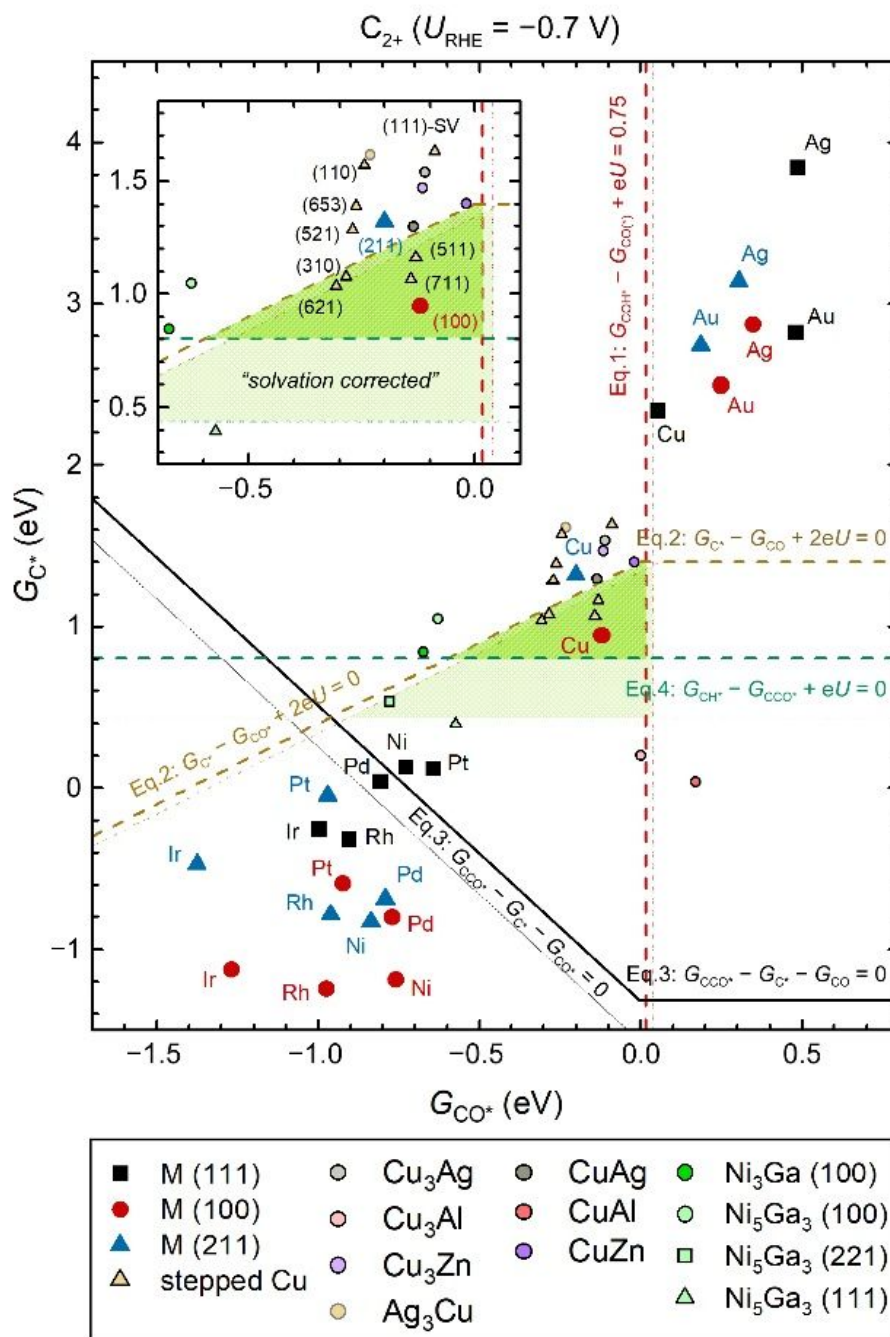
Figure 6. **(G_{CO*}, G_{C*}) selectivity map at U_{RHE} = −0.7 V (pH7).** The G_{CO*} and G_{C*} used herein are obtained through vacuum-level calculations for easy implementation. The C_2-selective region is highlighted in green. Various metallic and intermetallic systems are included with symbols as indicated in the legend. The detailed surface orientations and computational details can be found in the Supplementary Material. Square, circular, and triangular symbols correspond to surfaces with three-fold hollow sites, four-fold hollow sites, and under-coordinated step sites, respectively. Electrochemically driven processes are shown as dashed lines and the potential-independent C-CO coupling process is indicated with solid lines. The thin lines in light colors, as well as corresponding highlighted region in light green are shown to refer to solvation effects. Note that the U in the equations is referenced to RHE.

Clearly, the C_2 selectivity changes with applied potential and at -0.7 V vs. RHE, the above thermodynamic conditions form a triangular region (marked in green in **Figure 6**) where a decent overall $CO_{(2)}R$ rate to C_2 products can be obtained and where CCO* is thermodynamically favored over CH* formation. This map presents a powerful tool, as it is capable of qualitatively discerning C_1 and C_2 product selectivity across all metals. Remarkably, all known C_2 selective Cu facets fall near the center of the region at this potential. It is noteworthy that Cu(211) sits on the edge of the region, whereas Cu(111) is unable to catalyze $CO_{(2)}R$ to C_2 or C_1 at such low overpotential. Despite the simple approach based only on thermodynamic arguments, the depicted trend is in agreement with the sophisticated kinetics analysis used in the previous sections. In short, the thermodynamic selective map is sufficient to qualitatively describe the $CO_{(2)}R$ selectivity across a large span of materials space.

Furthermore, the maps at various potentials also shows the narrow potential window of opportunity to form C_2 products (**Figures S19–S20**). (100)-like facets are found to be essential for improving C_2 selectivity since the above narrow window does not include materials with dominant (111)-like facets (**Figures S21–S22**). These effects accentuate the challenge in identifying C_2-selective catalysts beyond Cu, Cu-based alloys, and intermetallics. Ag and Au do not form C_2 because of their poor C* binding energies. Strong-binding metals can easily reduce CO to C* but the C* on these surfaces is not as reactive as on more noble metals like Cu to enable the C-CO coupling step rather than CO adsorption. Very few candidates relevant from experimental results fall in the C_2-selective region, including Cu alloys with Zn,[7] Ag,[8] and Al,[10] Ni-Ga intermetallics,[51] as well as defective Cu[52] (modeled as Cu(111) with a single vacancy, denoted as (111)-SV).

While the CO dimerization pathway has been successful in describing the pH independent behavior of C_2 rates on Cu surfaces, we note in the following several observations that cannot easily be understood from a pathway involving CO dimerization, which on the other hand can be explained by the COH and OC-C pathway:

- Surface-carbon-induced deactivation of Cu catalysts during $CO_{(2)}R$[4, 53] can only be attained through coupling of atomic carbon and not through decomposition of CH_x species. This is because of the inability of Cu to break the C–H bond at room temperature,[54] hence, atomic carbon must be present as an intermediate during $CO_{(2)}R$, thus supporting the COH pathway.

- CO dimerization on Au exhibits a ΔG_{rxn} of only 0.50 eV (~0.50 eV lower than Cu) considering the same solvation and electric field conditions as on Cu. Hence, Au should in principle be a particularly selective catalyst toward C_2 products through the CO dimerization. This, however, has never been experimentally validated.

- Ni-rich $Ni_3Ga(100)$ and (111) surfaces were found unable to stabilize OCCO*. Hence, we do not expect CO dimerization to account for the observed C_2 production on Ni-Ga intermetallics.[51] The observed earlier onset potential for C_2 products on Ni-Ga intermetallics than found on Cu, can however be well understood based on the OC-C mechanism as shown in **Figure S19**.

Thus, the OC-C mechanism offers the ability to rationalize the above experimental observations with regards to material screening under neutral pH conditions, whereas the CO dimerization mechanism is more relevant for alkaline conditions. This suggests that understanding the role of atomic carbon in the $CO_{(2)}R$ provides a necessary insight into the reaction mechanism and paves the way for discovery of new materials. The insights developed with the OC-C mechanism enables us to propose several pathways for enhancing the $C_{2(+)}$ selectivity from $CO_{(2)}R$: (1) precise control of micro-/nanostructures of Cu catalysts to enhance the number of sites resembling the local environment on highly selective single-crystal Cu electrodes such as the Cu(511) and Cu(310) surfaces; (2) engineering of reaction microenvironments that increases the local availability of CO/CO_2, regulate the charge and electric field distribution, and modulate the water activity at the interface; (3) design of alloy/intermetallic catalysts with the desirable CO and C binding strengths on geometrically well-defined surface structures.

Conclusion

We have identified the relevant reaction pathways for $CO_{(2)}R$ towards further reduced C_1 (methane) and C_{2+} based on first principles reaction energetics and micro-kinetic modeling. We elucidated the role of atomic carbon as the key surface intermediate that directs the C_1/C_{2+} selectivity through two distinct competing reaction pathways. Our model enables quantification of experimentally observed activity/selectivity trends for $CO_{(2)}R$ on Cu at varying potentials and changes in surface orientation. We also demonstrated that with the two simple thermodynamic descriptors, CO and C binding strengths, a number of

experimental observations can be rationalized across a range of metal and metal alloy catalysts. In particular, four-fold hollow sites on Cu-like materials were identified as strongly C_{2+}-selective, however only within a narrow potential window. These insights enable us to identify the immense challenges associated with the search for new materials that are similar or even surpass Cu in terms of activity and selectivity.

Acknowledgements

References

1. P. De Luna, C. Hahn, D. Higgins, S. A. Jaffer, T. F. Jaramillo and E. H. Sargent, *Science*, 2019, **364**, eaav3506.
2. M. B. Ross, P. De Luna, Y. F. Li, C. T. Dinh, D. Kim, P. Yang and E. H. Sargent, *Nat. Catal.*, 2019, **2**, 648-658.
3. D. F. Gao, R. M. Aran-Ais, H. S. Jeon and B. R. Cuenya, *Nat. Catal.*, 2019, **2**, 198-210.
4. S. Nitopi, E. Bertheussen, S. B. Scott, X. Y. Liu, A. K. Engstfeld, S. Horch, B. Seger, I. E. L. Stephens, K. Chan, C. Hahn, J. K. Nørskov, T. F. Jaramillo and I. Chorkendorff, *Chem. Rev.*, 2019, **119**, 7610-7672.
5. Y. Y. Birdja, E. Perez-Gallent, M. C. Figueiredo, A. J. Gottle, F. Calle-Vallejo and M. T. M. Koper, *Nat. Energy*, 2019, **4**, 732-745.
6. C. W. Li, J. Ciston and M. W. Kanan, *Nature*, 2014, **508**, 504-507.
7. D. Ren, B. S. H. Ang and B. S. Yeo, *ACS Catal.*, 2016, **6**, 8239-8247.
8. E. L. Clark, C. Hahn, T. F. Jaramillo and A. T. Bell, *J. Am. Chem. Soc.*, 2017, **139**, 15848-15857.
9. C. G. Morales-Guio, E. R. Cave, S. A. Nitopi, J. T. Feaster, L. Wang, K. P. Kuhl, A. Jackson, N. C. Johnson, D. N. Abram, T. Hatsukade, C. Hahn and T. F. Jaramillo, *Nat. Catal.*, 2018, **1**, 764-771.
10. M. Zhong, K. Tran, Y. M. Min, C. H. Wang, Z. Y. Wang, C. T. Dinh, P. De Luna, Z. Q. Yu, A. S. Rasouli, P. Brodersen, S. Sun, O. Voznyy, C. S. Tan, M. Askerka, F. L. Che, M. Liu, A. Seifitokaldani, Y. J. Pang, S. C. Lo, A. Ip, Z. Ulissi and E. H. Sargent, *Nature*, 2020, **581**, 178-183.
11. F. S. Roberts, K. P. Kuhl and A. Nilsson, *Angew. Chem. Int. Ed.*, 2015, **54**, 5179-5182.
12. D. Kim, C. S. Kley, Y. F. Li and P. D. Yang, *Proc. Natl. Acad. Sci. U. S. A.*, 2017, **114**, 10560-10565.
13. K. Jiang, R. B. Sandberg, A. J. Akey, X. Y. Liu, D. C. Bell, J. K. Nørskov, K. R. Chan and H. T. Wang, *Nat. Catal.*, 2018, **1**, 111-119.
14. J. J. Lv, M. Jouny, W. Luc, W. L. Zhu, J. J. Zhu and F. Jiao, *Adv. Mater.*, 2018, **30**, 1803111.
15. M. R. Singh, Y. Kwon, Y. Lum, J. W. Ager and A. T. Bell, *J. Am. Chem. Soc.*, 2016, **138**, 13006-13012.
16. J. Resasco, L. D. Chen, E. Clark, C. Tsai, C. Hahn, T. F. Jaramillo, K. Chan and A. T. Bell, *J. Am. Chem. Soc.*, 2017, **139**, 11277-11287.
17. D. F. Gao, I. T. McCrum, S. Deo, Y. W. Choi, F. Scholten, W. M. Wan, J. G. G. Chen, M. J. Janik and B. R. Cuenya, *ACS Catal.*, 2018, **8**, 10012-10020.
18. J. Li, D. H. Wu, A. S. Malkani, X. X. Chang, M. J. Cheng, B. J. Xu and Q. Lu, *Angew. Chem. Int. Ed.*, 2020, **59**, 4464-4469.
19. S. C. Ma, M. Sadakiyo, R. Luo, M. Heima, M. Yamauchi and P. J. A. Kenis, *J. Power Sources*, 2016, **301**, 219-228.
20. C. T. Dinh, T. Burdyny, M. G. Kibria, A. Seifitokaldani, C. M. Gabardo, F. P. G. de Arquer, A. Kiani, J. P. Edwards, P. De Luna, O. S. Bushuyev, C. Q. Zou, R. Quintero-Bermudez, Y. J. Pang, D. Sinton and E. H. Sargent, *Science*, 2018, **360**, 783-787.
21. M. Jouny, W. Luc and F. Jiao, *Nat. Catal.*, 2018, **1**, 748-755.
22. F. Pelayo García de Arquer, C. T. Dinh, A. Ozden, J. Wicks, C. McCallum, A. R. Kirmani, D. H. Nam, C. Gabardo, A. Seifitokaldani, X. Wang, Y. C. Li, F. W. Li, J. Edwards, L. J. Richter, S. J. Thorpe, D. Sinton and E. H. Sargent, *Science*, 2020, **367**, 661-666.
23. A. D. Handoko, F. X. Wei, Jenndy, B. S. Yeo and Z. W. Seh, *Nat. Catal.*, 2018, **1**, 922-934.
24. E. L. Clark and A. T. Bell, *J. Am. Chem. Soc.*, 2018, **140**, 7012-7020.
25. K. L. Yang, R. Kas and W. A. Smith, *J. Am. Chem. Soc.*, 2019, **141**, 15891-15900.
26. Y. Hori, R. Takahashi, Y. Yoshinami and A. Murata, *J. Phys. Chem. B*, 1997, **101**, 7075-

7081.

27.   K. J. P. Schouten, Z. S. Qin, E. P. Gallent and M. T. M. Koper, *J. Am. Chem. Soc.*, 2012, **134**, 9864-9867.

28.   L. Wang, S. A. Nitopi, E. Bertheussen, M. Orazov, C. G. Morales-Guio, X. Y. Liu, D. C. Higgins, K. R. Chan, J. K. Nørskov, C. Hahn and T. F. Jaramillo, *ACS Catal.*, 2018, **8**, 7445-7454.

29.   F. Calle-Vallejo and M. T. M. Koper, *Angew. Chem. Int. Ed.*, 2013, **52**, 7282-7285.

30.   J. H. Montoya, C. Shi, K. Chan and J. K. Nørskov, *J. Phys. Chem. Lett.*, 2015, **6**, 2032-2037.

31.   W. J. Luo, X. W. Nie, M. J. Janik and A. Asthagiri, *ACS Catal.*, 2016, **6**, 219-229.

32.   H. Xiao, T. Cheng and W. A. Goddard, *J. Am. Chem. Soc.*, 2017, **139**, 130-136.

33.   T. Cheng, H. Xiao and W. A. Goddard, *Proc. Natl. Acad. Sci. U. S. A.*, 2017, **114**, 1795-1800.

34.   A. J. Garza, A. T. Bell and M. Head-Gordon, *ACS Catal.*, 2018, **8**, 1490-1499.

35.   X. Y. Liu, P. Schlexer, J. P. Xiao, Y. F. Ji, L. Wang, R. B. Sandberg, M. Tang, K. S. Brown, H. J. Peng, S. Ringe, C. Hahn, T. F. Jaramillo, J. K. Nørskov and K. R. Chan, *Nat. Commun.*, 2019, **10**, 32.

36.   S. Ringe, E. L. Clark, J. Resasco, A. Walton, B. Seger, A. T. Bell and K. Chan, *Energy Environ. Sci.*, 2019, **12**, 3001-3014.

37.   Y. G. Kim, A. Javier, J. H. Baricuatro, D. Torelli, K. D. Cummins, C. F. Tsang, J. C. Hemminger and M. P. Soriaga, *J. Electroanal. Chem.*, 2016, **780**, 290-295.

38.   M. Tang, H. Peng, P. S. Lamoureux, M. Bajdich and F. Abild-Pedersen, *Appl. Catal. B-Environ.*, 2019, **279**, 119384.

39.   K. P. Kuhl, E. R. Cave, D. N. Abram and T. F. Jaramillo, *Energy Environ. Sci.*, 2012, **5**, 7050-7059.

40.   K. Chan and J. K. Nørskov, *J. Phys. Chem. Lett.*, 2015, **6**, 2663-2668.

41.   M. L. Ng, F. Abild-Pedersen, S. Kaya, F. Mbuga, H. Ogasawara and A. Nilsson, *Phys. Rev. Lett.*, 2015, **114**, 246101.

42.   M. T. Tang, Z. W. Ulissi and K. R. Chan, *J. Phys. Chem. C*, 2018, **122**, 14481-14487.

43.   X. Y. Liu, J. P. Xiao, H. J. Peng, X. Hong, K. Chan and J. K. Nørskov, *Nat. Commun.*, 2017, **8**, 15438.

44.   J. J. Kim, D. P. Summers and K. W. Frese, *J. Electroanal. Chem.*, 1988, **245**, 223-244.

45.   C. T. Campbell, *ACS Catal.*, 2017, **7**, 2770-2779.

46.   B. Zijlstra, X. Zhang, J. X. Liu, I. A. W. Filot, Z. Y. Zhou, S. G. Sun and E. J. M. Hensen, *Electrochim. Acta*, 2020, **335**, 135665.

47.   Y. Hori, I. Takahashi, O. Koga and N. Hoshi, *J. Mol. Catal. A-Chem.*, 2003, **199**, 39-47.

48.   J. K. Nørskov, J. Rossmeisl, A. Logadottir, L. Lindqvist, J. R. Kitchin, T. Bligaard and H. Jonsson, *J. Phys. Chem. B*, 2004, **108**, 17886-17892.

49.   P. S. Lamoureux, A. R. Singh and K. R. Chan, *ACS Catal.*, 2019, **9**, 6194-6201.

50.   X. Wang, J. Ferreira de Araújo, W. Ju, A. Bagger, H. Schmies, S. Kühl, J. Rossmeisl and P. Strasser, *Nat. Nanotechnol.*, 2019, **14**, 1063-1070.

51.   D. A. Torelli, S. A. Francis, J. C. Crompton, A. Javier, J. R. Thompson, B. S. Brunschwig, M. P. Soriaga and N. S. Lewis, *ACS Catal.*, 2016, **6**, 2100-2104.

52.   M. Liu, M. X. Liu, X. M. Wang, S. M. Kozlov, Z. Cao, P. De Luna, H. M. Li, X. Q. Qiu, K. Liu, J. H. Hu, C. K. Jia, P. Wang, H. M. Zhou, J. He, M. Zhong, X. Z. Lan, Y. S. Zhou, Z. Q. Wang, J. Li, A. Seifitokaldani, C. T. Dinh, H. Y. Liang, C. Q. Zou, D. L. Zhang, Y. Yang, T. S. Chan, Y. Han, L. Cavallo, T. K. Sham, B. J. Hwang and E. H. Sargent, *Joule*, 2019, **3**, 1703-1718.

53.   Z. Weng, X. Zhang, Y. S. Wu, S. J. Huo, J. B. Jiang, W. Liu, G. J. He, Y. Y. Liang and H. L. Wang, *Angew. Chem. Int. Ed.*, 2017, **56**, 13135-13139.

54.   S. Wang, V. Petzold, V. Tripkovic, J. Kleis, J. G. Howalt, E. Skulason, E. M. Fernandez,

21

B. Hvolbaek, G. Jones, A. Toftelund, H. Falsig, M. Bjorketun, F. Studt, F. Abild-Pedersen, J. Rossmeisl, J. K. Nørskov and T. Bligaard, *Phys. Chem. Chem. Phys.*, 2011, **13**, 20760-20765.
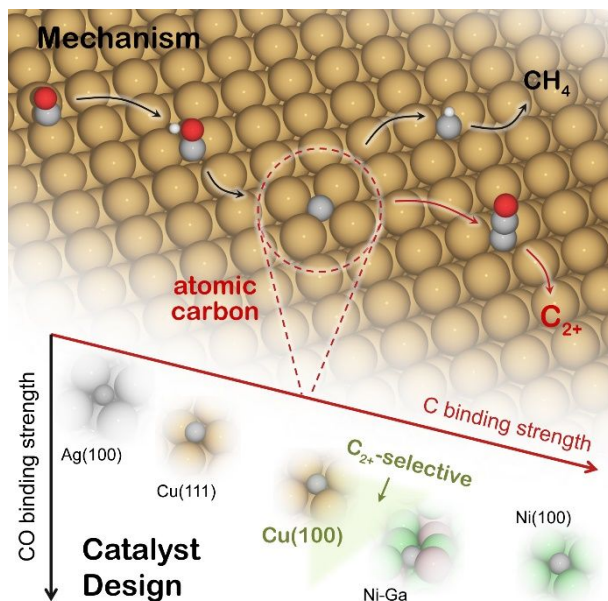
Atomic carbon presents as a key intermediate steering the single-carbon and multi-carbon product selectivity during electrochemical carbon mono-/dioxide reduction and appropriate binding strengths of CO and C, combined with the four-fold geometry of an active site, constitute the fundamental design principles for exploring selective catalysts toward multi-carbon products.